

Novel Chemical Treatment of Porous Titanium Structures for Nanotextured Surface and Bioactive Behavior

*Original*

Novel Chemical Treatment of Porous Titanium Structures for Nanotextured Surface and Bioactive Behavior / Ferraris, Sara; Alidoost, Dario; Spriano, Silvia; Torres, Yadir; Beltran, Anamaria. - In: ADVANCED ENGINEERING MATERIALS. - ISSN 1527-2648. - 26:20(2024). [10.1002/adem.202400866]

*Availability:*

This version is available at: 11583/2995533 since: 2024-12-17T16:25:09Z

*Publisher:*

John Wiley and Sons

*Published*

DOI:10.1002/adem.202400866

*Terms of use:*

This article is made available under terms and conditions as specified in the corresponding bibliographic description in the repository

*Publisher copyright*

(Article begins on next page)

# Novel Chemical Treatment of Porous Titanium Structures for Nanotextured Surface and Bioactive Behavior

Sara Ferraris,\* Dario Alidoost, Silvia Spriano, Yadir Torres, and AnaMaria Beltran

Macroporous titanium structures are of interest in bone reconstruction because of their reduced modulus of elasticity (compared to bulk titanium), possibility of being colonized by cells, and biocompatibility. However, they are not bioactive and are not able to actively facilitate bone ingrowth or reduce bacterial adhesion. In the present research, work porous titanium scaffolds with different features (porosity 30–60 vol% and pore size 100–200 or 355–500  $\mu\text{m}$ ) are obtained by the space holder technique. Samples are characterized using optical microscopy, computed tomography, scanning electron microscopy (SEM), and X-ray diffraction. Moreover, the theoretical elastic modulus and yield strength are calculated. A patented chemical treatment, able to produce a bioactive nanotextured oxide layer, has been optimized and successfully applied, for the first time, to structures with 50 vol% porosity and 100–200  $\mu\text{m}$  pore size (as the most promising for bone substitution due to the biomechanical and biofunctional balance). Bare and modified samples are characterized using field emission SEM, zeta potential measurements, and in vitro bioactivity tests (soaking in simulated body solution) to evaluate the effectiveness of the surface chemical treatment.

## 1. Introduction

Bone grafts are necessary in case of bone nonunions, malunions, or bone defects associated with tumors, osteonecrosis, orthopedic surgery (e.g., trauma treatment, spinal fusion, and

endoprostheses), dental implants, and cranial or maxillofacial applications.<sup>[1]</sup> The use of bone grafts is continuously increasing, and currently, there are 2 million bone grafting procedures performed per year in the world.<sup>[1]</sup>

A proper design of the scaffold (porosity, pore size, material, processing, and surface treatment) is required to obtain bone substitutes able to match clinical needs.<sup>[2]</sup>

The main solutions proposed for bone grafting are autografts, allografts, and synthetic grafts. Autografts and allografts have the highest similarity with the host bone but have significant issues related to limited availability and eventual morbidity.<sup>[3]</sup> Synthetic grafts must be designed to mimic the complex characteristics of bone and to be physiologically osseointegrated. Mainly, synthetic grafts should have proper mechanical properties (to guarantee stable

fixation, sustain loads, and avoid stress shielding phenomena), suitable porosity (to assure tissue ingrowth and tailored mechanical properties), selected material (to match mechanical and biocompatibility/bioactivity requirements), and proper surface features (to mimic the extracellular matrix environment and to support bone integration).<sup>[3]</sup>

Even if lower than other metals, Young's modulus ( $E$ ) of titanium is still larger than the cortical bone, generating stress shielding, and therefore, the potential failure of implants.<sup>[4,5]</sup> One potential solution is the use of a porous structure since it reduces Young's modulus to be more like the bone. In addition to that, pores improve osseointegration since depending on the percentage of the pores, size, and interconnection, pores can facilitate the bone ingrowth and vascularization of the implants. However, it is still necessary to treat the surface (modification of the texture and/or chemistry of the surface) to improve osseointegration; it means the chemical union between implant and bone.


Among different techniques to fabricate porous structures, additive manufacturing is gaining increasing interest in the fabrication of customized bone implants and grafts due to its ability to modulate different features such as porosity, shape, dimension, composition (in situ alloying), and mechanical properties.<sup>[6–8]</sup> However, some issues, such as surface finishing, fatigue resistance, and biological response, are still not completely resolved and proper surface modifications of additive-manufactured titanium implants are still under investigation.<sup>[6]</sup>

On the other hand, the use of powder metallurgy, and, particularly, the space holder technique permits the manufacture of

S. Ferraris, S. Spriano  
Department of Applied Science and Technology  
Politecnico di Torino  
Turin 10129, Italy  
E-mail: sara.ferraris@polito.it

D. Alidoost  
Advanced Joining Technologies Interdepartmental Laboratory  
Politecnico di Torino (J-TECH@POLITO)  
Turin 10129, Italy

Y. Torres, A. M. Beltran  
Departamento de Ingeniería y Ciencia de los Materiales y del Transporte  
Escuela Politécnica Superior  
Universidad de Sevilla  
Sevilla 41011, Spain

 The ORCID identification number(s) for the author(s) of this article can be found under <https://doi.org/10.1002/adem.202400866>.

© 2024 The Author(s). Advanced Engineering Materials published by Wiley-VCH GmbH. This is an open access article under the terms of the Creative Commons Attribution-NonCommercial-NoDerivs License, which permits use and distribution in any medium, provided the original work is properly cited, the use is non-commercial and no modifications or adaptations are made.

DOI: 10.1002/adem.202400866

structures in which the percentage of porosity and pore range size can be tailored, and it is equally interesting and competitive with additive manufacturing. Furthermore, it is an economical, easy, and repetitive technique.

According to these requirements, we selected to work on titanium porous grafts considering the already well-proven good outcome of titanium bone implants and the possibility of treating the titanium surface to get osteoconductive and osteoinductive ability.

In the past, the authors obtained a nanotextured topography on porous scaffolds by means of argon irradiation through direct irradiation synthesis.<sup>[9]</sup>

In the present research work, titanium porous pieces were obtained through the space holder technique with different porosities and pore dimensions. For the first time, a surface chemical treatment was applied to the optimized 3D structures to obtain a nanotextured topography, on both the outer and inner pore surfaces, as well as the surface among pores and bioactive behavior (induced precipitation of hydroxyapatite in contact with the body fluids). The chemical treatment is a patented process on plane and fully dense samples and is well characterized, and its peculiar features (bioactivity, ability to promote osteoblast adhesion and differentiation, reduced bacterial adhesion, and reduced macrophage adhesion)<sup>[10–14]</sup> are extremely promising. This is why we decided to combine it with a porous titanium structure aimed at bone substitution. The chemical treatment is based on the immersion of samples in different chemical solutions. So, it is suitable for porous constructs and easily scalable to industrial production without needing complex or expensive equipment. In this research work, process parameters have been optimized to combine the designed scaffold porosity with surface micro- and nano-features due to the chemical etching.

## 2. Experimental Section

### 2.1. Fabrication of Titanium Substrates

In this work, commercially pure titanium (c.p. Ti) powder was used to manufacture fully dense (conventional powder metallurgy, PM) and porous substrates (space holder technique, SH), with ammonium bicarbonate particles, as spacer particles (BA) (NH<sub>4</sub>HCO<sub>3</sub>). The c.p. Ti (grade IV, according to ASTM:F67-13) was provided by SEJONG Materials Co. Ltd. (Seoul, Korea) with a particle size distribution  $d_{[50]} = 23.3 \mu\text{m}$ ,<sup>[15]</sup> while the BA of 99% purity was supplied by Cymit Quimica S.L. (Barcelona, Spain). Porous titanium substrates were fabricated using different volume percentages (30, 40, 50, and 60 vol%) and range sizes (100–200 and 355–500  $\mu\text{m}$ ) of spacer particles. C.p. Ti powder was mixed with the BA spacer particles (desirable vol% and range of size) and pressed at 800 MPa on an Instron 5505 machine. The BA was then removed in two stages (60 °C and 110 °C) for 12 h each, before sintering the substrates at 1250 °C for 2 h in a high vacuum atmosphere ( $\approx 10^{-5}$  mbar). On the other hand, fully dense samples were fabricated by PM route by pressing at 1300 MPa and then sintering at 1300 °C (same high vacuum conditions). These substrates were used as references.

A summary of the prepared samples and their acronyms is reported in Table 1.

**Table 1.** Summary of the prepared samples and their acronyms.

Acronym	Porosity [vol%]	Pore size (size of spacer holder particles) [ $\mu\text{m}$ ]
30%_100–200	30	100–200
30%_355–500	30	355–500
40%_100–200	40	100–200
40%_355–500	40	355–500
50%_100–200	50	100–200
50%_355–500	50	355–500
60%_100–200	60	100–200
60%_355–500	60	355–500

### 2.2. Metallographic Characterization

After sintering, a standard metallography procedure (grinding and mechano-chemical polishing) was performed on the surface before the acquisition of images using a Nikon Eclipse MA100 N optical microscope. At least five images of each substrate were analyzed to evaluate total porosity ( $P_T$ ). In addition, the equivalent diameter of the pores,  $D_{eq}$ , and the shape factor,  $F_f$ , were also determined from these images. For image analysis (IA), Image-ProPlus 6.2 software (Mediacibernectic, Bethesda, MD, USA) was used. By Archimedes' method,<sup>[16]</sup> total and interconnected porosity ( $P_i$ ) as well as density were also determined.

### 2.3. Theoretical Evaluation of Young's Modulus and Yield Strength

Mechanical behavior was estimated using equations reported in the literature. In fact, the mechanical properties (stiffness,  $E$  and yield strength,  $\sigma_y$ ) of the substrates were calculated using fit equations, which relate the porosity characteristics to mechanical behavior. In particular, the dynamic Young's modulus ( $E_d$ ) was calculated according to Equation (1):<sup>[17]</sup>

$$E_d = E_{Ti} \cdot (e^{-0.02 \cdot P_T}) - 0.03 \cdot E_{Ti} \quad (1)$$

where  $E_{Ti}$  is the Young's modulus for bulk Ti ( $\approx 110 \text{ GPa}$ )<sup>[18,19]</sup> and  $P_T$  is the percentage of total porosity of the sample. This equation is valid for c.p. Ti samples with 20–60% total porosity, which is the porosity range of the studied substrates.

For comparison, Nielsen's approximation was also used to estimate Young's modulus according to Equation (2), based on the total porosity and shape factor:<sup>[20]</sup>

$$E_N = \frac{E_{Ti} \cdot (1 - \frac{P_T}{100})^2}{1 + (F_f - 1) \cdot \frac{P_T}{100}} \quad (2)$$

where  $E_{Ti}$  is Young's modulus for bulk grade IV c.p. Ti ( $\approx 110 \text{ GPa}$ ),  $P_T$  is the percentage of total porosity of the sample, and  $F_f$  is the shape factor, calculated from IA.

Finally,  $\sigma_y$  was also calculated according to Equation (3):<sup>[17]</sup>

$$\frac{\sigma_y}{\sigma_{Ti}} = (1.2018 \cdot e^{-0.043 \cdot P_i}) \quad (3)$$

where  $\sigma_{Ti}$  is the yield strength of c.p. Ti ( $\approx 650 \text{ GPa}$ )<sup>[21]</sup> and  $P_i$  is the percentage of interconnected porosity of the sample.

## 2.4. Computed Tomography Characterization

The distribution of porosity in the structures was analyzed in a nondestructive way by means of computed tomography (Tomograph Fhg, customized X-ray tomography system for non-destructive analyses). The optimized X-ray emission parameters of 250 kV and 30  $\mu$ A were selected which provided the high resolution of 10  $\mu$ m. The images registered with the computed tomography were elaborated with VGStudiomax35 to create a 3D model of the sample. For the porosity analysis, the VGEasyPore algorithm was applied to investigate the diameter and volumes of the pores. The VGEasyPore uses subvoxel accuracy that enables high levels of mimics of the pore's parameters such as radius, diameter, volume, and sphericity. In this method, the voxels are identified as defects based on the local gray value of the material in relation to the background (surrounding air). In the analysis, a gray value difference compared to the surrounding air larger than 10 was considered. The histograms demonstrate the distribution of the diameter and volume of the pores.

## 2.5. X-Ray Diffraction (XRD)

The crystallographic structure of porous structures was investigated by means of X-ray diffraction (XRD) measurements (PANalytical X'Pert Pro PW 3040 160 Philips) and compared with the data obtained from titanium disks cut from dense bars (ASTM B348, Gr2, Titanium Consulting and Trading) XRD spectra were analyzed by means of XPERT High Score software.

## 2.6. Surface Chemical Treatment

Porous structures with 50% porosity and pore size in the 100–200  $\mu$ m range 50%\_100–200 (selected for their suitable bio-mechanical and biofunctional balance) underwent a patented chemical treatment (CT) aimed at the development of a nanotextured surface layer rich in hydroxyl groups able to impart bioactive behavior (ability to promote hydroxyapatite precipitation in vitro and bone bonding in vivo).<sup>[10–12]</sup> In brief, the treatment foresees a first acid etching in diluted hydrofluoric acid to remove the native oxide layer, followed by a controlled oxidation in hydrogen peroxide at 60 °C under shaking. The process parameters (acid concentration—1 M and etching time—1'30") were optimized in order to develop a uniform oxide layer on the outer and inner surfaces of the porous structure without altering their macroscopic features.

Chemically treated porous structures with 50% porosity and 100–200  $\mu$ m pore size will be named 50%\_100–200-CT from now on.

## 2.7. Surface Morphological Characterization

The development of surface nanotexture was assessed by means of field emission scanning electron microscopy (FESEM, SUPRATM 40, Zeiss) on porous structures after the chemical treatment.

In order to investigate the development of the nanotexture inside the inner pores of the structure, coarse grinding of treated samples was performed for the removal of material from the

surface. Samples were then washed in ethanol in an ultrasonic bath, dried under compressed air, and observed with the earlier cited FESEM instrument.

## 2.8. Zeta Potential and Isoelectric Point Measurements

The zeta potential of bare and chemically treated porous structures was investigated by means of an electrokinetic analyzer for solid surfaces (SurPASS, Anton Paar) equipped with a cylindrical cell.

0.001 M KCl was used as an electrolyte (starting pH 5.5). Basic and acid titration curves were obtained, on the same sample, by the addition of 0.05 M NaOH or 0.05 M HCl through the instrument's automatic titration unit. The sample was abundantly washed with ultrapure water between the two measures.

## 2.9. In Vitro Bioactivity Tests

In vitro bioactivity, the ability to induce hydroxyapatite precipitation in simulated physiological conditions, was investigated by soaking samples in simulated body fluid (SBF) at 37 °C up to 14 days. SBF was prepared according to the protocol proposed by Kokubo.<sup>[22]</sup> At the end of the soaking, period samples were gently washed in ultrapure water, let dry in air, and analyzed by means of scanning electron microscopy (SEM, JEOL, JCM 6000 plus) equipped with energy-dispersive spectroscopy (EDS, JEOL, JED 2300).

# 3. Results

## 3.1. Metallographic Characterization

Macro-images of the substrates (**Figure 1**) showed the homogeneity of the surface for the different percentages of porosity and the size of the pore range of the spacer particles. Optical images of the substrates (**Figure 2**) revealed the porosity. Two different ranges of pore sizes were observed: microporosity generated during the sintering process (<50  $\mu$ m), which was also present in the fully dense sample, and the macropores due to the spacer particles.

IA of these images was performed, and results were reported in **Table 2**, corroborating the expected porosity from the fabrication procedure. Slight differences compared to Archimedes' method could be found because measures were performed on a two-dimensional surface and not on the total volume of the substrates, as well as few interferences were due to the experimental fabrication. The highest vol. % porosity was not so homogenous since spacer particles could be agglomerated during the fabrication procedure. The higher the porosity, the higher the value of  $P_i$  reached, and this is even more true with a larger size of the spacer particles.

## 3.2. Theoretical Evaluation of Young's Modulus and Yield Strength

Mechanical properties could be estimated from the porosity percentage as it was aforementioned. **Table 3** summarizes the mechanical data calculated based on data from IA analyses,



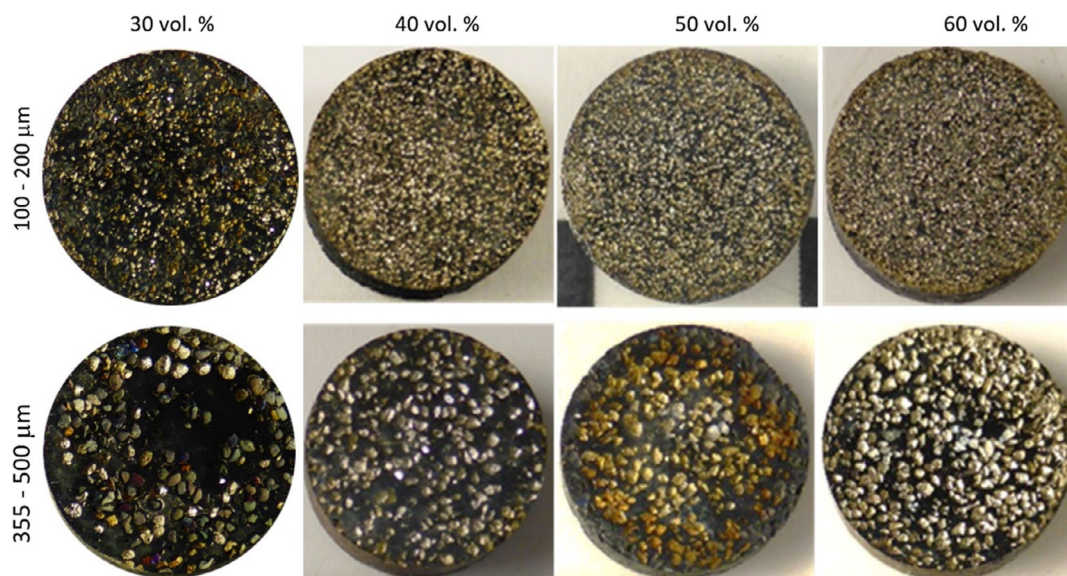


**Figure 1.** Macro-images of the samples (12 mm diameter).

evidencing the efficacy of the space holder technique to decrease Young's modulus and yield stress, as higher porosity percentage and pores range size. In general, for the same porosity, mechanical properties were lower as higher pores range size. According to these results, the 50 vol% substrates were more suitable to replace cortical bone, especially for the pores size 100–200  $\mu\text{m}$ , since the obtained values are close to the natural bone<sup>[23,24]</sup> and, from previous studies of the authors, these structures present the best biocompatibility and osteoblasts adhesion and proliferation.<sup>[25]</sup> For this reason, these samples were selected for surface treatment and further characterizations.

### 3.3. Computed Tomography Characterization

**Figure 3** reports an example of computed tomography scan images and data obtained on the 50%\_100–200 sample.

Computed tomography scan analyses showed a homogeneous distribution of porosity without a large number of evident macro-defects. The pore dimension was in accordance with the one set with the selection of the space holder dimension and with metallographic characterization. The mean volume of the pores resulted around 6000–10 000  $\mu\text{m}^3$ .

### 3.4. X-Ray Diffraction (XRD)

The XRD spectrum of the 50%\_100–200 sample is reported in **Figure 4** compared with the one of a bulk commercially pure titanium polished disk.

The spectra are very similar, and all the peaks (even the peaks at around 73°, 108°, and 118° visible only on the porous sample) can be assigned to alpha hexagonal titanium. In the case of porous titanium, the peak at 38.4° can be dubious because it is a peak characteristic of both alpha hexagonal and beta cubic titanium. It cannot be excluded to be correlated with the presence of beta titanium due to the sintering treatment carried out at a

high temperature (1250 °C) during the production phase. The absence of the other peaks typical of this crystallographic structure excluded the presence of a large quantity of this second phase. No specific peaks of titanium oxide can be evidenced on the spectrum of the porous sample evidencing that eventual oxidation during the thermal treatment is negligible and limited to the outermost surface layer.

### 3.5. Surface Morphology

The surface morphology before and after the chemical treatment was assessed by FESEM to verify the preservation of the macropores dimensions and morphology as well as the development of the nanotexture inside and outside pores. FESEM images of the bare and treated porous structures are shown in **Figure 5**.

It can be observed that the chemical treatment did not damage the macroporosity of the structure (**Figure 5a,c**) and that a nanotexture was homogeneously developed on the surface after the treatment, while no nanometric features were visible on the untreated sample (**Figure 5b,d**). The nanotexture is well developed on treated samples on both the external surfaces and the inner pores (**Figure 5f**). This nanotexture was analogous to that already investigated by the authors on dense titanium disks and implants chemically treated in the same way.<sup>[26]</sup>

### 3.6. Isoelectric Points and Zeta Potential Titration Curves

The zeta potential titration curves of porous and chemically treated porous titanium samples were measured by the zeta potential electrokinetic measurements (**Figure 6**).

The values of the isoelectric points were obtained as the pH values where the measured zeta potential was null or as the intersection of the curve with the abscissa axis by interpolation when it was at a too low pH value to be directly measured. The isoelectric point of porous titanium is 3.13, slightly more acidic than the

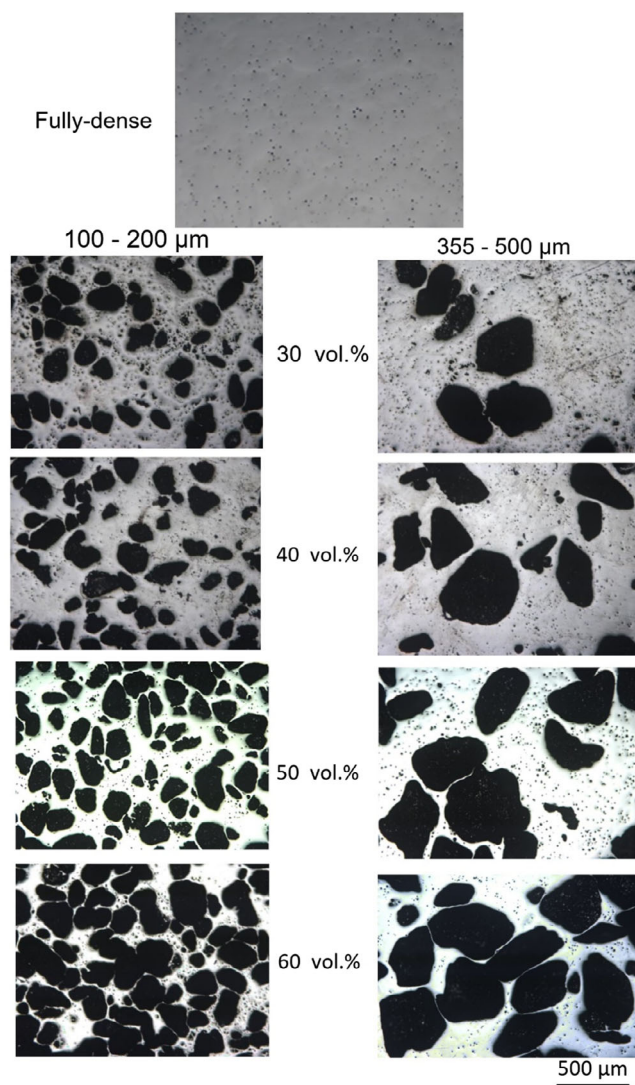


**Figure 2.** Optical microscopy images of the porous c.p. Ti substrates and the fully dense sample. Common scale bar for all the images.

**Table 2.** Experimental parameters measured by IA ( $F_f$ ) and Archimedes' ( $P_T$ ,  $P_i$ ) method.

Sample	IA		Archimedes'	
	$P_T$ [%]	$F_f$	$P_T$ [%]	$P_i$ [%]
Fully dense	$0.03 \pm 0.03$	—	$2.11 \pm 0.21$	—
30%_100–200	$26.74 \pm 2.31$	$0.30 \pm 0.19$	$30.75 \pm 0.70$	$13.45 \pm 0.31$
30%_355–500	$29.99 \pm 4.01$	$0.50 \pm 0.14$	$30.13 \pm 0.69$	$19.55 \pm 0.45$
40%_100–200	$37.37 \pm 0.52$	$0.36 \pm 0.22$	$39.59 \pm 0.91$	$27.80 \pm 0.64$
40%_355–500	$40.13 \pm 2.23$	$0.31 \pm 0.24$	$34.88 \pm 0.80$	$18.14 \pm 0.42$
50%_100–200	$47.51 \pm 2.23$	$0.40 \pm 0.19$	$43.65 \pm 1.00$	$32.25 \pm 0.74$
50%_355–500	$49.12 \pm 2.46$	$0.29 \pm 0.30$	$48.92 \pm 1.12$	$36.55 \pm 0.84$
60%_100–200	$55.18 \pm 3.50$	$0.42 \pm 0.18$	$55.16 \pm 1.26$	$51.31 \pm 1.17$
60%_355–500	$56.13 \pm 3.40$	$0.26 \pm 0.30$	$57.08 \pm 1.31$	$49.71 \pm 1.14$

**Table 3.** Mechanical properties estimated from IA data.

Sample	Estimated dynamic Young's modulus, $E_d$ [GPa]		Estimated $\sigma_y$ [MPa]
	$E_d$ (Equation (1))	$E_N$ (Equation (2))	$\sigma_y$ (Equation (3))
30%_100–200	$62.6 \pm 3.0$	$73.6 \pm 6.7$	$438 \pm 40$
30%_355–500	$56.6 \pm 2.7$	$63.1 \pm 5.2$	$337 \pm 32$
40%_100–200	$49.1 \pm 2.4$	$56.8 \pm 4.7$	$236 \pm 23$
40%_355–500	$49.2 \pm 3.2$	$59.0 \pm 5.0$	$358 \pm 33$
50%_100–00	$41.7 \pm 2.0$	$46.1 \pm 3.8$	$194 \pm 18$
50%_355–500	$37.9 \pm 1.8$	$43.6 \pm 3.6$	$162 \pm 15$
60%_100–200	$33.3 \pm 1.6$	$36.1 \pm 3.0$	$86 \pm 8$
60%_355–500	$29.8 \pm 1.4$	$31.4 \pm 2.4$	$92 \pm 8$

one reported in the literature<sup>[27]</sup> and previously measured by the authors<sup>[28]</sup> (4.0–4.5) for dense titanium and its alloys. This difference can be explained by the oxide layer formed during the thermal treatment of the scaffold. After the chemical treatment, a shift of the isoelectric point toward more acidic values (not measurable by the instrument but calculated as close to 2 by interpolation) was observed, according to what was previously observed by the authors on chemically treated titanium disks.<sup>[29,30]</sup> This acidic shift is correlated with the formation of a specific type of surface oxide layer during the etching enriched with acidic functional groups (OH groups). Moreover, a significant plateau in the basic region (with onset at pH of at about 5.6) can be observed on the treated sample. As previously reported by the authors, it can be associated with the presence of surface acidic groups (OH groups) easily deprotonated even at low pH values.<sup>[29,30]</sup> The onset of the plateau was shifted to a more acidic value when compared to the untreated scaffold because of the different chemical reactivity of the OH groups.

The big jump around pH 5 on the untreated sample is due to the difference in the zeta potential value between the beginning of the acid and basic titrations. This difference can be explained considering sample reactivity in the acidic region, confirmed by the high standard deviation around pH4. It means that when the basic titration started, the surface of the samples was a bit altered by the contact with the acid solutions.

On the chemically treated samples, this jump was reduced due to the more stable oxide layer developed on the surface. A very lower alteration of the samples occurred during the acidic titration. The moderate valley around pH 3–4 for the treated sample can be attributed to the usual standard deviation in this range. Even if it is reduced, compared to the untreated sample, at low pH a moderate reaction of the material with the solution can be supposed and documented by the increase in the standard deviation values in the very acidic range. The high surface area of a porous structure is expected to make each chemical reaction much more evident.

### 3.7. In Vitro Bioactivity

**Figure 7** shows the morphology and chemical composition of 50%\_100–200 and 50%\_100–200\_CT after 14 days of soaking in SBF.

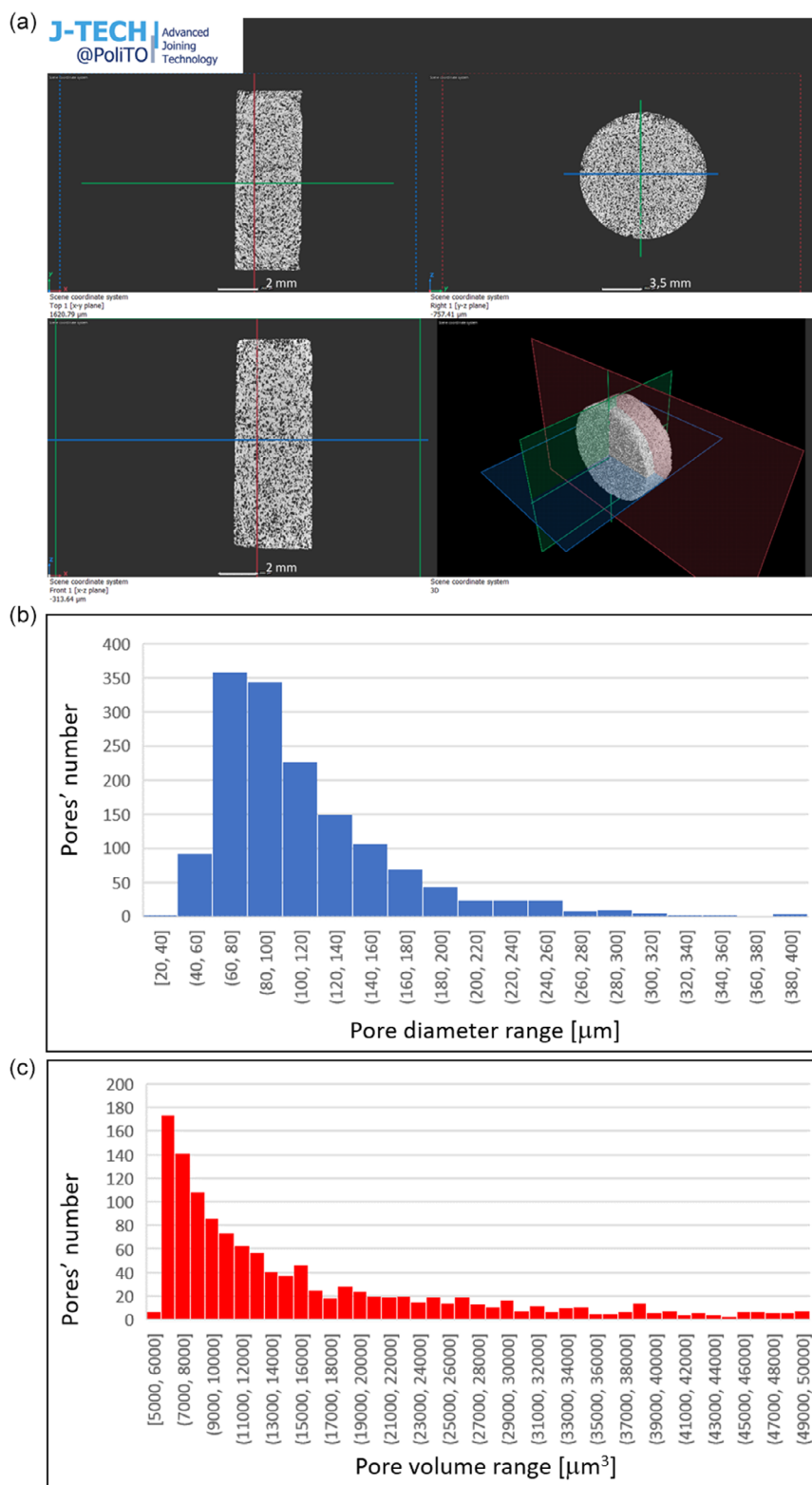


**Figure 3.** Computed tomography scan data of 50%\_100–200 sample: a) 3D images of the porous structure, b) distribution of pore diameters from computed tomography scan acquisition, and c) pore volume from computed tomography scan acquisition.



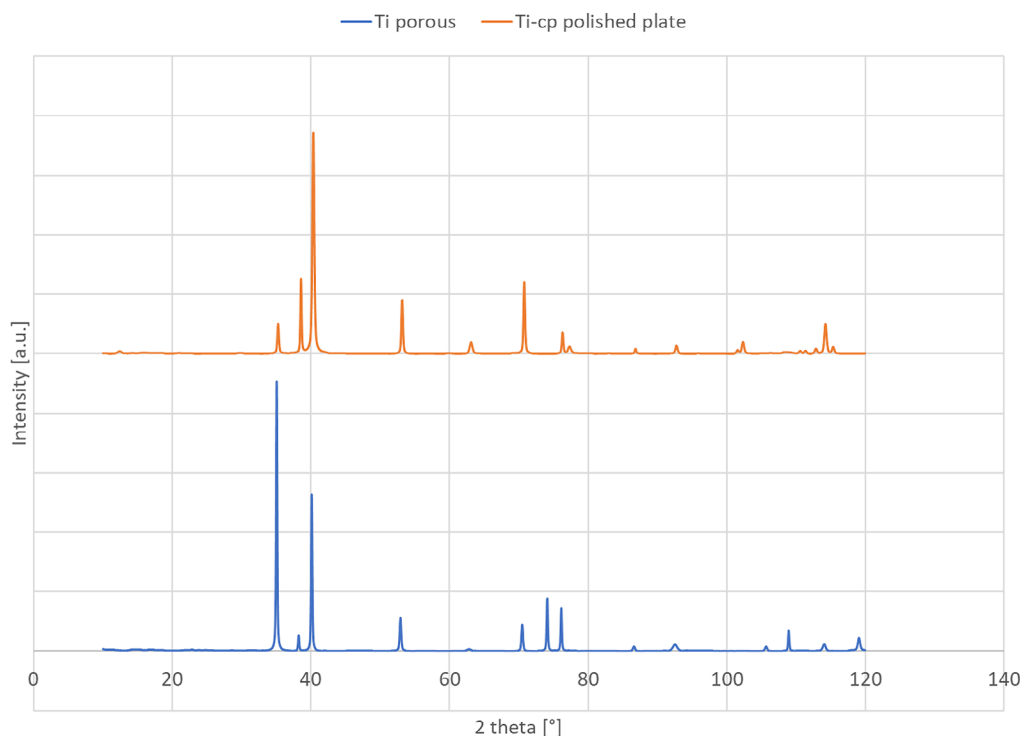


**Figure 4.** XRD diffractograms of 50%\_100–200 sample.

A significant increase in calcium and phosphorous can be observed on the chemically treated sample, compared to the bare one, after 14 days of soaking in SBF. Moreover, a lot of particles with the typical morphology of hydroxyapatite and rich in Ca and P can be noticed on the treated surface after 14 days in SBF. These particles were not present in the untreated sample. Moreover, it can be underlined that these particles are present also in the inner pores.

#### 4. Discussion

Porous titanium structures were successfully obtained by the space holder technique. The average porosity designed through space holder selection (size and amount) was confirmed by optical observations on the metallographic sections of the obtained samples. The homogeneity of pore distribution was assessed by both optical observations (on metallographic sections) and computed tomography (volumetric analysis) evidencing the absence of a large number of macro-defects.

The porosity resulted interconnected, and this feature is of crucial importance in the case of porous structures designed for bone substitution in order to guarantee proper perfusion of gases and nutrients and bone integration.

The modulation of porosity allowed to successfully tailor the Young modulus of the construct with E values of about  $\frac{1}{4}$  of the titanium one for constructs with 60% of porosity. This strategy allowed obtaining bone substitutes with an elastic modulus closer to the one of bone, with a potential positive outcome on stress shielding effects.

Mechanical properties of the porous titanium scaffolds were previously experimentally evaluated by the authors by means of uniaxial compression tests. An inverse relationship between porosity/pore size and elastic modulus/yield strength was demonstrated.<sup>[31]</sup> The value of the elastic modulus was modulated between 20 and 23 GPa for a 50% porosity scaffold varying the pore size from 100–200  $\mu\text{m}$  to 355–500  $\mu\text{m}$ <sup>[25]</sup> and properly matching the typical value of bone. As for the yield strength, values between 127 and 98 MPa were obtained for a 50% porosity scaffold varying the pore size from 100–200 to 355–500  $\mu\text{m}$ .<sup>[25,32]</sup> These values are almost one-fifth of the yield strength of fully dense titanium. Even if these numbers are quite low for bone substitution, this problem could be compensated by the growth of bone tissue toward the inner part of the implant.<sup>[32]</sup>

The experimental evaluation of Young's modulus in porous materials is controversial. In this work, the mechanical behavior is estimated, using fitting equations proposed by the authors in previous works, using experimental data from porous titanium samples, manufactured by different routes. Despite their good adjustment, we cannot forget that there are many parameters that can explain the discrepancy between experimental and theoretical values, for example, the quality of the necks between particles, the porosity itself (percentage, size, and shape factor), the stiffness of the testing machine, etc. In this context, it is essential to note that Young's modulus measurements from uniaxial compression tests are significantly lower than dynamic measurements. Greiner et al.<sup>[33]</sup> associated this discrepancy with superelastic deformation within the linear elastic range of NiTi materials. Stiffness measured by ultrasonic technique decreases with increasing porosity in agreement with Eshelby's



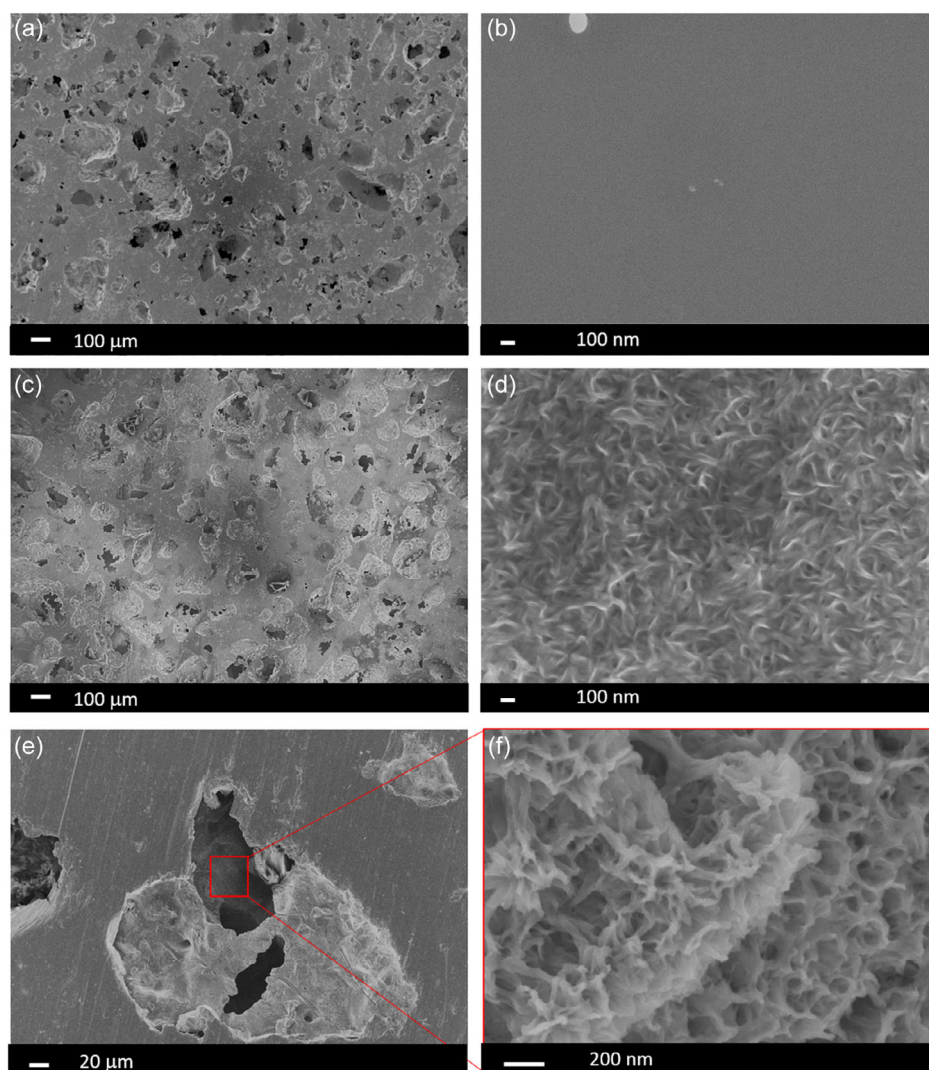


**Figure 5.** FESEM images, a) 50%\_100–200 low magnification (100×), b) 50%\_100–200 high magnification (100000×), c) 50%\_100–200-CT low magnification (100×), d) 50%\_100–200-CT high magnification (100000×), e) 50%\_100–200-CT low magnification (500×) after grinding for the exposition of inner pores, and f) 50%\_100–200-CT high magnification (100000×) inside exposed inner pore.

elasticity-based theory for closed, spherical porosity. We reported a similar trend for C.P. Ti obtained by a conventional powder metallurgy process,<sup>[34]</sup> as well as in recent work<sup>[35]</sup> developed with space holder (NaCl). These authors related this difference to the testing machine stiffness in which the mechanical system and sample were considered as two springs in series. Furthermore, it must be remembered that Ti matrix is different at each cross section of the cylindrical sample during a compression test; the material collapse starts at the section with the lowest Ti content. In works such as those mentioned earlier, the reliability and certainty of ultrasound measurements were validated by comparison with a well-known and accepted pore elasticity model, such as that of Nielsen.<sup>[36]</sup>

As previously demonstrated by the authors,<sup>[37,38]</sup> structures with 50% porosity and a pore size of 100–200 μm obtained by the space holder technique are the ones that best suit to replace the cortical bone ( $\sigma_y = 150\text{--}180\text{ MPa}$  and  $E = 20\text{--}25\text{ GPa}$ ). In the

case of 50% porosity and small pore size, there is a perfect combination of mechanical strength and Young's modulus. Young's modulus is almost the same as the cortical bone one allowing the avoidance of stress shielding phenomena. Pore dimension in the 100–200 μm range has been reported as optimal for the formation of vascularized bone,<sup>[39]</sup> osteoblast adhesion, and regeneration of mineralized bone.<sup>[24]</sup> Moreover, micropores (due to sintering) are beneficial for protein absorption.<sup>[24]</sup> Based on these results, the structures obtained with 50% porosity and a spacer of 100–200 μm were chosen as the substrate for the subsequent chemical surface treatment. This is the key novelty of this research. Even if one of the key points for using porous constructs is that osseointegration is facilitated because a great fixing surface is provided, as-prepared porous structures both by 3D printing or powder metallurgy are characterized by poor surface finishing.<sup>[40]</sup> It is well known that surface roughness, chemistry, energy, and morphology have a key role in the mechanism of

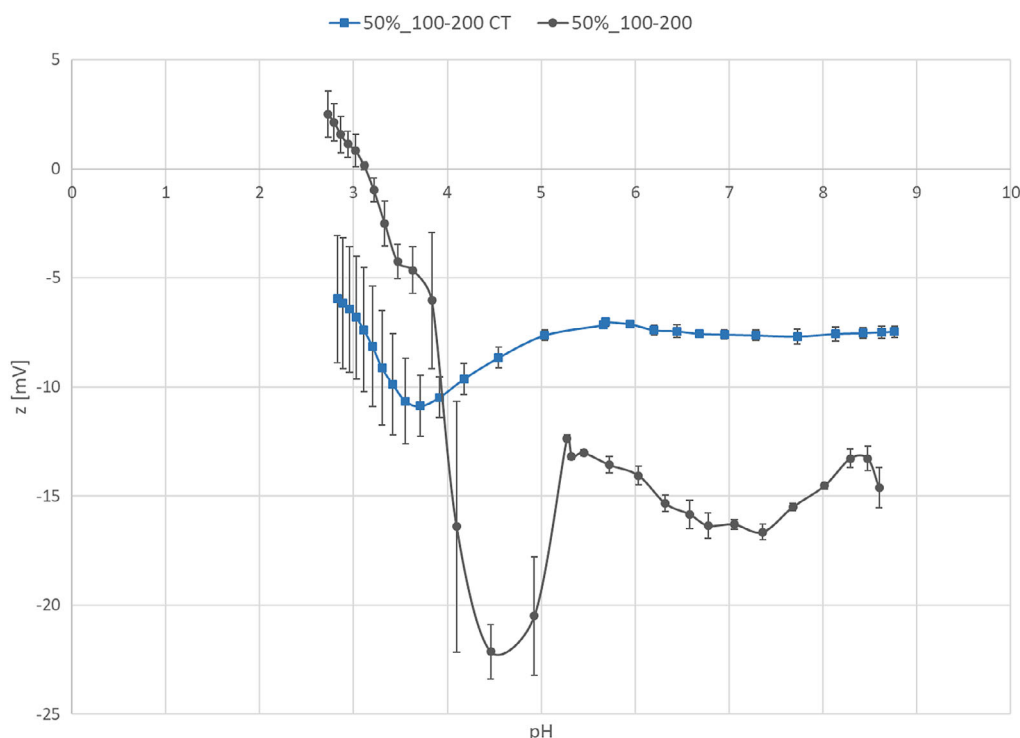


**Figure 6.** Zeta potential titration curves for 50%\_100–200 and 50%\_100–200 CT.

focal adhesions of osteoblasts and contact osteogenesis, as well as in the bioactive behavior (induction of precipitation of hydroxyapatite). The surface treatments already assessed for dense titanium implants are not suitable for 3D constructs just the way they are:<sup>[6]</sup> the inner porous structure can be not accessible to the deposition of a coating, the fatigue resistance of the component must be strictly preserved, and time and costs of the treatments should not vanish the economic advantages of additive manufacturing or powder metallurgy. Lastly, the risk of infection of an implant with high surface area and inner niches with low circulation of the physiological liquids is potentially high.<sup>[40]</sup>

A chemical treatment, based on etching/oxidizing baths, allows the modification of both outer and inner pore surfaces resulting to be suitable for porous structures. Common chemical etching for dense titanium bone implants is performed in strong acid mixtures which are not suitable for a porous 3D construct exposing a large surface area to corrosion.<sup>[41]</sup> Proper optimization of surface process parameters is needed, and the here-developed process allowed the maintenance of macro- and micro-features with the superposition of a homogeneous nanotexture on the surface. Differently from previous chemical treatments performed by the authors on porous structures, which resulted in microtexture,<sup>[42]</sup> here surface features are at the nanoscale. The obtained nanotextured oxide layer was rich in hydroxyl groups as evidenced by zeta potential results.<sup>[11,12]</sup> The presence of the peculiar morphology and reactive chemical groups induced the ability to promote hydroxyapatite precipitation during the *in vitro* soaking of the samples in SBF. The mechanism goes through deprotonation of the acidic OH groups at physiological pH, adsorption of calcium ions from the physiological

fluids, and consequent adsorption of the phosphate groups.<sup>[30]</sup> This behavior is related to surface ability to promote bone bonding *in vivo*.<sup>[43]</sup> Moreover, it has been shown by the authors that this chemical treatment can favor osteoblast differentiation and reduce biofilm formation.<sup>[13]</sup> The presence of a multiscale topography with micro- and nanoscale roughness overlapped with macroporosity had a positive role in the involved mechanisms of bioactivity and osseointegration.<sup>[44]</sup>

Differently from acid etching reported in the literature for porous titanium structures,<sup>[42,45]</sup> characterized by surface micro-roughness, the here-proposed treatment produces a multi-scale surface topography (micro- and nanotextures) coupled with significant hydroxylation and bioactive behavior. The bioactivity of the here-reported chemical treatment is slower than the one obtained by other chemical treatments (such as the NaOH-based ones),<sup>[30,45]</sup> because of a different mechanism. In this case, apatite was formed through electrostatic attraction instead of ion exchange. An important difference is that the interface between the formed apatite and the surface is more stable over time when this mechanism occurs.<sup>[46]</sup> Moreover, the here-proposed chemical treatment does not require expensive equipment and long treatment time and is easily scalable in the production process of medical implants.<sup>[12,47]</sup>

In conclusion, the here-produced 3D titanium graft showed a lot of the requested features for a good bone substitute: Young's modulus was close to that of the bone, the size and interconnection of the pores were suitable for the permeation of nutrients and gases, the percentage of the porosity was in the range requested for vascularized bone in-growth, and the surface induced precipitation of hydroxyapatite. This construct is suitable

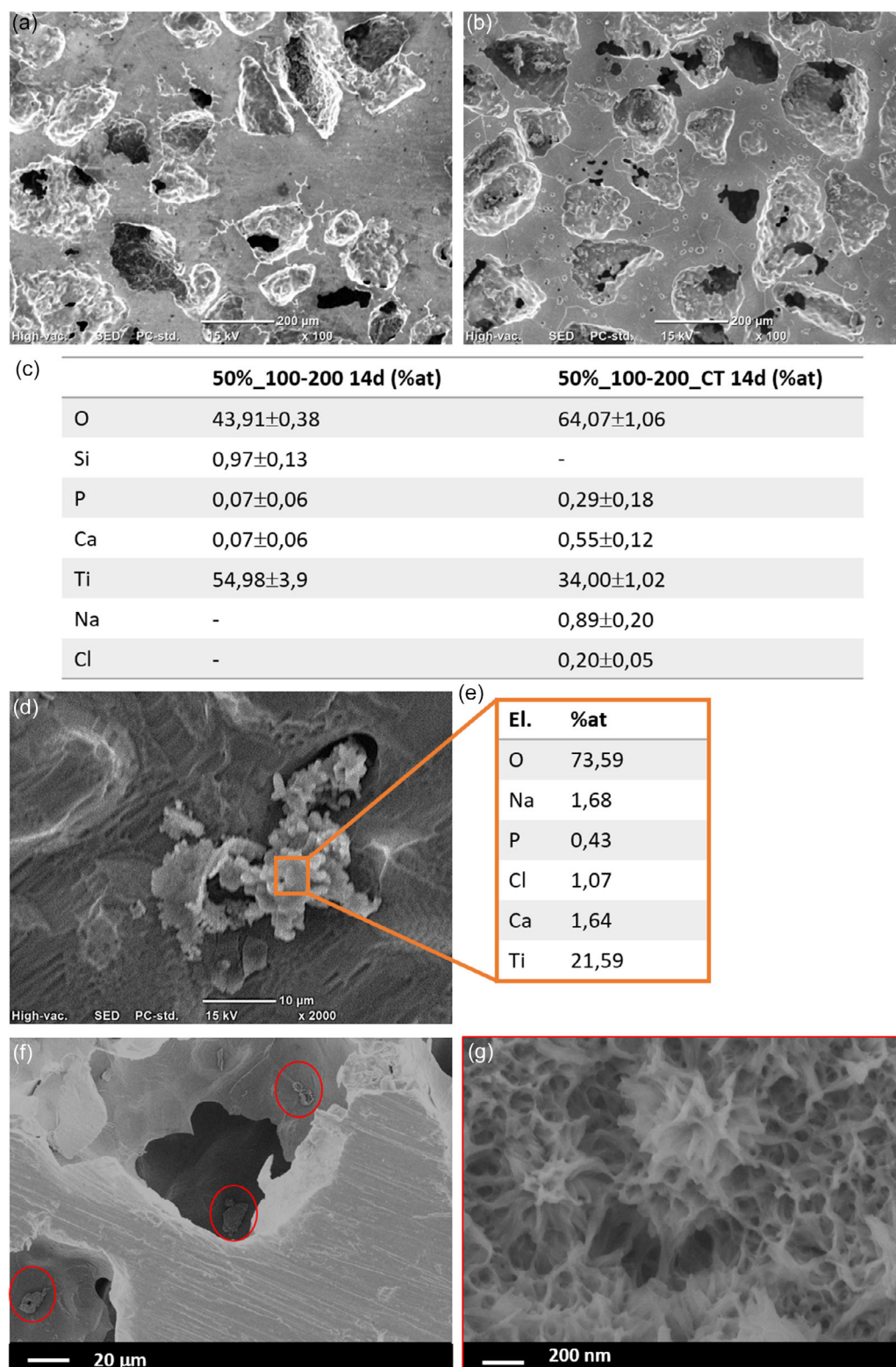


**Figure 7.** SEM-EDS analyses of 50%\_100–200 and 50%\_100–200\_CT after 14 days in SBF. a) Surface morphology of the 50%\_100–200 sample, b) surface morphology of the 50%\_100–200\_CT samples, c) EDS analyses of the two surfaces (at%), d) detail of precipitate on the surface of the 50%\_100–200\_CT samples, e) EDS analysis of the precipitate, f) low magnification (1000×) FESEM image of the 50%\_100–200 CT after exposition of inner pores, precipitated particles into inner pores evidenced by red circles, and g) high magnification (100000×) FESEM image of a particle into the inner pore.



for contact osteogenesis, and the risk of peri-implant infection is potentially reduced by a surface not prone to bacteria adhesion. The coupling of a bioactive and nanotextured titanium surface to a 3D titanium porous graft was a further step toward the state-of-the-art of bone substitutes. Cell cultures will be performed in future work to verify if the potential benefits of this 3D construct are validated in a biological environment.

## 5. Conclusion

Porous titanium scaffolds with porosity ranging from 30% to 60% and pore size in the 100–200 or 355–500  $\mu\text{m}$  range and interconnected porosity were successfully obtained by the space holder technique. Structures with 50% porosity and 100–200  $\mu\text{m}$  pore size were considered the most suitable for bone substitution purposes and underwent a patented chemical treatment to obtain a nanotextured oxide layer. The chemical treatment was properly optimized to preserve macroporosity and develop nanotexture on the surface outside and inside the pores. Modified surfaces were able to induce hydroxyapatite precipitation in vitro.

## Acknowledgements

Open access publishing facilitated by Politecnico di Torino, as part of the Wiley - CRUI-CARE agreement.

## Conflict of Interest

The authors declare no conflict of interest.

## Data Availability Statement

The data that support the findings of this study are available from the corresponding author upon reasonable request.

## Keywords

bioactivity, chemical treatment, nanotexture, porous structure, titanium

Received: April 8, 2024

Revised: July 4, 2024

Published online: August 2, 2024

- [1] C. E. Gillman, A. C. Jayasuriya, *Mater. Sci. Eng. C* **2021**, 130, 112466.
- [2] G. L. Koons, M. Diba, A. G. Mikos, *Nat. Rev. Mater.* **2020**, 5, 584.
- [3] S. Wu, X. Liu, K. W. K. Yeung, C. Liu, X. Yang, *Mater. Sci. Eng. R* **2014**, 80, 1.
- [4] M. Kaur, K. Singh, *Mater. Sci. Eng. C* **2019**, 102, 844.
- [5] K. Pałka, R. Pokrowiecki, *Adv. Eng. Mater.* **2018**, 20, 1700648.
- [6] S. Ferraris, S. Spriano, *Metals* **2021**, 11, 1343.
- [7] F. Trevisan, F. Calignano, A. Aversa, G. Marchese, M. Lombardi, S. Biamino, D. Ugués, D. Manfredi, *J. Appl. Biomater. Funct. Mater.* **2018**, 16, 57.
- [8] M. Salmi, *Materials* **2021**, 14, 191.
- [9] A. Civantos, A. Mesa-Restrepo, Y. Torres, A. R. Shetty, M. K. Cheng, C. Jaramillo-Correa, T. Aditya, J. P. Allain, *J. Biomed. Mater. Res.* **2023**, 111, 1850.
- [10] S. Spriano, E. Vernè, S. Ferraris, *Eur. Patent* **2007**, 10, 2214732.
- [11] S. Ferraris, S. Spriano, G. Pan, A. Venturello, C. L. Bianchi, R. Chiesa, M. G. Faga, G. Maina, E. Vernè, *J. Mater. Sci. Mater. Med.* **2011**, 22, 533.
- [12] S. Ferraris, A. Bobbio, M. Miola, S. Spriano, *Surf. Coat. Tech.* **2015**, 276, 374.
- [13] S. Ferraris, A. Cochis, M. Cazzola, M. Tortello, A. Scalia, S. Spriano, L. Rimondini, *Front. Bioeng. Biotechnol.* **2019**, 7, 103.
- [14] J. Barthes, M. Cazzola, C. Muller, C. Dollinger, C. Debry, S. Ferraris, S. Spriano, N. E. Vrana, *Mater. Sci. Eng. C* **2020**, 112, 110845.
- [15] Y. Torres, P. Trueba, J. Pavón, I. Montealegre, J. A. Rodríguez-Ortiz, *Mater. Des.* **2014**, 63, 316.
- [16] ASTM C373-14(2014), Standard Test Method for Water Absorption, Bulk Density, Apparent Porosity, and Apparent Specific Gravity of Fired Whiteware Products, Ceramic Tiles, and Glass Tiles, in ASTM Int., West Conshohocken, PA **2014**, <https://doi.org/10.1520/C0373-14>.
- [17] S. Lascano, C. Arévalo, I. Montealegre-Melendez, S. Muñoz, J. A. Rodríguez-Ortiz, P. Trueba, Y. Torres, *Appl. Sci.* **2019**, 9, <https://doi.org/10.3390/app9050982>.
- [18] H. Shen, L. C. Brinson, *Int. J. Solids Struct.* **2007**, 44, 320.
- [19] Y. Li, C. Yang, H. Zhao, S. Qu, X. Li, Y. Li, *Materials* **2014**, 7, 1709.
- [20] L. F. Nielsen, *Mater. Struct. Constr.* **1996**, 31, 651.
- [21] T. Imwinkelried, *J. Biomed. Mater. Res. A* **2007**, 81, 964.
- [22] T. Kokubo, H. Takadama, *Biomaterials* **2006**, 27, 2907.
- [23] R. Oftadeh, M. Perez-Viloria, J. C. Villa-Camacho, A. Vaziri, A. Nazarian, *J. Biomech. Eng.* **2015**, 137, 0108021.
- [24] N. Abbasi, S. Hamlet, R. M. Love, N.-T. Nguyen, *J. Sci.: J. Sci.-Adv. Mater. Dev.* **2020**, 5, 1.
- [25] A. Civantos, A. M. Beltrán, C. Domínguez-Trujillo, M. D. Garvi, J. Lebrato, J. A. Rodríguez-Ortiz, F. García-Moreno, J. V. Cauich-Rodríguez, J. J. Guzman, Y. Torres, *Metals* **2019**, 9, 1039.
- [26] S. Lumetti, E. Manfredi, S. Ferraris, S. Spriano, G. Passeri, G. Ghiacci, G. Macaluso, C. Galli, *J. Mater. Sci. Mater. Med.* **2016**, 27, 68.
- [27] B. S. Bal, M. N. Rahaman, *Acta Biomater.* **2012**, 8, 2889.
- [28] S. Spriano, V. Sarath Chandra, A. Cochis, F. Uberti, L. Rimondini, E. Bertone, A. Vitale, C. Scolaro, M. Ferrari, F. Cirisano, G. Gautier di Confienzo, S. Ferraris, *Mater. Sci. Eng. C* **2017**, 74, 542.
- [29] S. Ferraris, M. Cazzola, V. Peretti, B. Stella, *Front. Bioeng. Biotechnol.* **2018**, 6, 60.
- [30] S. Ferraris, S. Yamaguchi, N. Barbani, M. Cazzola, C. Cristallini, M. Miola, E. Vernè, S. Spriano, *Acta Biomater.* **2020**, 102, 468.
- [31] B. Begines, C. Arevalo, C. Romero, Z. Hadzhieva, A. R. Boccaccini, Y. Torres, *ACS Appl. Mater. Interfaces* **2022**, 14, 15008.
- [32] A. M. Beltrán, A. Civantos, C. Dominguez-Trujillo, R. Moriche, J. A. Rodríguez-Ortiz, F. García-Moreno, T. J. Webster, P. H. Kamm, A. Mesa Restrepo, Y. Torres, *Metals* **2019**, 9, 995.
- [33] C. Greiner, S. M. Oppenheimer, D. C. Dunand, *Acta Biomater.* **2005**, 1, 705.
- [34] Y. Torres, J. J. Pavón, I. Nieto, J. A. Rodríguez, *Met. Mater. Trans. B* **2011**, 42, 891.
- [35] Y. Torres, J. J. Pavón, J. A. Rodríguez, *J. Mater. Process. Technol.* **2012**, 212, 1061.
- [36] L. F. Nielsen, *J. Am. Ceram. Soc.* **1984**, 67, 93.
- [37] P. Trueba, C. Navarro, J. A. Rodríguez-Ortiz, A. M. Beltrán, F. J. García-García, Y. Torres, *Surf. Coat. Tech.* **2021**, 408, 126796.
- [38] A. Civantos, M. Giner, P. Trueba, S. Lascano, M.-J. Montoya-García, C. Arévalo, M.Á. Vázquez, J. P. Allain, Y. Torres, *Metals* **2020**, 10, 696.
- [39] D. Gao, A. U. Ernst, X. Wang, L. Wang, W. Liu, M. Ma, *Adv. Eng. Mater.* **2022**, 11, 2200922.



- [40] A. Rodríguez-Contreras, M. Punset, J. A. Calero, F. J. Gil, E. Ruperez, J. M. Manero, *J. Mater. Sci. Technol.* **2021**, 76, 129.
- [41] G. Singh, *J. Med. Dent. Sci.* **2018**, 17, 49.
- [42] A. Civantos, C. Domínguez, R. J. Pino, G. Setti, J. J. Pavón, E. Martínez-Campos, F. J. García García, J. A. Rodríguez, J. P. Allain, Y. Torres, *Surf. Coat. Tech.* **2019**, 368, 162.
- [43] S. Fujibayashi, M. Neo, H.-M. Kim, T. Kokubo, T. Nakamura, *Biomaterials* **2003**, 24, 1349.
- [44] A. Sotniczuk, H. Garbacz, *Adv. Eng. Mater.* **2021**, 23, 2000909.
- [45] T. Kawai, M. Takemoto, S. Fujibayashi, H. Akiyama, M. Tanaka, S. Yamaguchi, D. K. Pattanayak, K. Doi, T. Matsushita, T. Nakamura, T. Kokubo, S. Matsuda, *PLoS One* **2014**, 9, e88366.
- [46] S. Ferraris, S. Yamaguchi, N. Barbani, C. Cristallini, G. Gautier di Confengo, J. Barberi, M. Cazzola, M. Miola, E. Vernè, S. Spriano, *Mater. Sci. Eng. C* **2020**, 116, 111238.
- [47] T. Lai, J. L. Xu, X. Cao, L. Z. Bao, J. M. Luo, Y. Z. Huang, *J. Mater. Res. Tech.* **2021**, 14, 202.